



Research paper

Ultra- ordered array of CuCo_2S_4 microspheres on co-doped nitrogen, sulfur-porous graphene sheets with superior electrochemical performance for supercapacitor application

Fatemeh Heidari Gourji^{*}, Dhayalan Velauthapillai^{*}, Mansoureh Keykhaei

Department of Computer Science, Electrical Engineering and Mathematical Sciences, Western Norway University of Applied Sciences, Innalsveien 28, 5063 Bergen, Norway



ARTICLE INFO

Article history:

Received 21 March 2022

Received in revised form 2 June 2022

Accepted 4 June 2022

Available online xxxx

Keywords:

Hybrid CuCo_2S_4 /NS-pG composite
Co-doped NS-porous graphene oxide
3D CuCo_2S_4 microspheres
Supercapacitor application

ABSTRACT

Engineering and designing unique morphologies is a smart way to tune the characteristics of the material. Here, in this work, beyond the existing knowledge, we have focused on developing novel methods for synthesis of high performance CuCo_2S_4 (CCS) and Graphene nanostructured material for supercapacitor applications. We first developed a rich mesoporous CCS-graphene structure, and for further enhancement of electrochemical performance, we incorporated nitrogen(N) and sulfur(S) into the graphene (NS-pG) framework. Further, through a controllable synthesis procedure dominated by nucleation and growth mechanism, we could obtain a highly ordered array of CuCo_2S_4 microspheres on the surface of graphene sheets confirmed by FESEM images. Successful material modifications have led to realize a novel CuCo_2S_4 /NS-pG composite structure with remarkable electrochemical performance. The as-obtained, tuned hybrid CuCo_2S_4 /NS-pG composite structure exhibited great surface area, excellent structural stability, and high electrical conductivity due to its modified morphology. Based on these unique advantages, the hybrid CuCo_2S_4 /NS-pG composite-based electrode revealed exceptional specific capacitance of 1357.8 F g^{-1} at 1 A g^{-1} , superior cycle performance of 95.9% after 5000 cycles, and distinguished maximum energy and power density of $80.59 \text{ W h kg}^{-1}$ and $10479.53 \text{ W kg}^{-1}$, respectively, which are superior to the performance of any reported CuCo_2S_4 electrodes.

© 2022 western norway university of applied sciences. Published by Elsevier Ltd. This is an open access article under the CC BY license (<http://creativecommons.org/licenses/by/4.0/>).

1. Introduction

Energy storage and energy production as two technological issues of human societies should be tackled in an eco-friendly way (Zhang et al., 2016). Supercapacitors (SCs) as an efficient and green electrochemical energy storage devices have drawn a wide attention because of their superior qualities (Zhang et al., 2015; Chen et al., 2021). The unique capabilities of mixing the advantages of both batteries and capacitors in SCs, make them as one of the high-performance energy-saving candidates (Zhu et al., 2013; Xu et al., 2016). SCs have numerous remarkable advantages such as high-power density, quick charge-discharge cycles, wide operating temperature, safety, low maintenance cost, prolong and stable cycle life (Isacfranklin et al., 2021; Kumar et al., 2021). There are two main classes of SCs based on their storage criteria: (i) electrochemical double layer supercapacitors (EDLCs), and (ii) pseudocapacitors (Zhang et al., 2015). In EDLCs, the charges store and release at the boundary surface of electrode/electrolyte by

physical adsorption/desorption process of ions meaning that in these type of SCs faradic redox reactions are not happening (Mohanty et al., 2021). Carbonaceous materials such as graphene, activated carbon (AC), carbon aerogel, carbon nanotubes (CNTs) are the most-used electrode materials for EDLCs (Zhang et al., 2015; Mohanty et al., 2021). In pseudocapacitors, electrical energy is obtained by faradic process through the highly reversible redox reaction or intercalations which is occurring on the surface of electrodes (Mohanty et al., 2021; Wu et al., 2021). Single transition metal oxides or hydroxides such as MnO_2 , RuO_2 are well known pseudocapacitors. Also, conducting polymers e.g., polypyrrole (PPy) and polyaniline (PANI) are showing pseudocapacitive properties (Wu et al., 2021).

However, due to the rapid self-discharge and low energy density, it is not possible to use the SCs as the primary energy source (Kumar et al., 2021; Amiri et al., 2021; Acharya et al., 2021b). To tackle these challenges, it is necessary to synthesize novel materials and design new morphologies to improve electrochemical performance and energy density. For this aim, in recent years, mixed transitional metal sulfides (MTMS) such as CuCo_2S_4 , NiCo_2S_4 , ZnCo_2S_4 , MnCo_2S_4 , CoNi_2S_4 known as being analogous to mixed transitional metal oxides (MTMO) (CuCo_2O_4 ,

^{*} Corresponding authors.

E-mail addresses: Fatemeh.Heidari.Gourji@hvl.no (F. Heidari Gourji), Dhayalan.Velauthapillai@hvl.no (D. Velauthapillai).

NiCo₂O₄, ZnCo₂O₄, MnCo₂O₄, CoNi₂O₄) have received a great interest because of their superb redox reversibility, conductivity and capacitance (Zhang et al., 2015; Yu and Lou, 2018; Geng et al., 2018; Chen et al., 2019). In comparison with single metal sulfides, binary metal sulfides (BMSSs), as a class of MTMS have drawn enormous attention for energy storage application because of their large redox reaction sites as well as high electrical conductivity (Geng et al., 2018; Sahoo et al., 2017; Askari et al., 2020).

Carbon derivatives, especially graphene-based materials, have been widely explored as electrode material in SCs due to their excellent structural, physical, and morphological properties (Tian et al., 2021). However, the experimentally obtained capacitance of graphene-based EDLCs is usually 100–200 F g⁻¹ which is far lower than the theoretical capacitance (520 F g⁻¹) (Chen et al., 2021; Liu et al., 2010; Zhu et al., 2014; Wang et al., 2015). The low capacitance of graphene is attributed to the strong π - π and van der Waals (vdW) interactions between graphene sheets which causing to restacking the sheets into graphite-like powders or thicker films (Kong et al., 2018). Also, due to their harsh synthetic condition such as Hummers' method (Pham et al., 2013), and large amount of oxygen-containing functional groups, the conductivity of graphene sheets is not as high as it is expected (Kong et al., 2018; Sun et al., 2011). Therefore, to tailor the graphene properties effectively, and also retain the large surface area (2630 m² g⁻¹) (Zhu et al., 2010) of graphene, two basic complementary approaches have been established by researchers: the first approach is designing of different morphologies. For example, producing holey graphene nanosheets is an important strategy for obtaining high specific surface area while benefiting ion diffusion. The abundant in-plane pores promote the ions transport and allow ions to approach the internal surface area of the electrodes resulting in higher power density of SCs (Hooch Antink et al., 2018; Kong et al., 2016). For example, Ma et al. synthesized pRGO through the facile one-pot microwave-assisted method, which exhibited 568.5 F g⁻¹ at 1 A g⁻¹ (Ma et al., 2021). Sethi et al. prepared porous graphene-NiO nanocomposite using simple solvothermal method, which showed a specific capacitance of 511 F g⁻¹ at scan rate of 5 mV s⁻¹ (Sethi et al., 2021). Tiruneh et al. synthesized NiCo₂S₄@holey Graphene hydrogel (HGH) through the solvothermal and hydrothermal methods, which showed high specific capacitance of 1000 F g⁻¹ at 0.5 A g⁻¹ (Tiruneh et al., 2018). The second solution is incorporation of certain heteroatoms such as nitrogen (N), sulfur (S), and boron (B) in carbon matrix (Wang et al., 2015; Zhang et al., 2014). Recent studies showed that substitutional doping of graphene with heteroatoms could considerably enhance the host material's electronic conductivity, mechanical strength, chemical stability, and surface activity (Kannan et al., 2014; Arvas et al., 2021). Specifically, it has been proven that the electronegativity difference between the carbon atoms and doped heteroatoms increases the surface polarity, resulting in higher capacitive performance (Tang et al., 2015; Wang et al., 2009). These properties are essential for energy storage applications. So far, nitrogen has been reported as the most prominent doping heteroatom in the carbon framework. The lone pair electrons in nitrogen atom can induce negative charge which leads to improved electron transfer ability (Kannan et al., 2014; Coros et al., 2020). However, compared to single-atom doping of carbon, dual doping enhances the synergetic effects and improve the capacitive behavior of carbon (Wang et al., 2015; Mehare et al., 2018). Doping of N is preferential for regulating the electronic properties of graphene, while sulfur has received increasing interest due to its larger size and its polarizable electron pairs, which results in higher chemical activity (Wang et al., 2015; Kiciński et al., 2014).

CuCo₂S₄ (CCS) is one of the MTMSs popular material with thiospinel crystal structure and *Fd3m* space group. DFT analysis

have showed (Oda et al., 1995; Li et al., 2017) that CCS is a p-type semiconductor with a bandgap value of around 0.47 eV meaning that this material possess of intrinsically metal-like excellent conductive characteristics. Compared to other MTMSs, CCS is the most widely studied electrode material among all the copper-containing binary sulfides (Lu et al., 2020). However, this material often suffers from poor cycle performance (Li et al., 2019) Therefore, preparing a graphene-based hybrid anode material is an effective strategy, which not only improves the conductivity, but also alleviates volume expansion and increases the surface area leading to higher power and energy density (Li et al., 2019).

In this study, through a facile and environmentally friendly solvothermal approach, we prepared hybrid CuCo₂S₄/NS-pG (CCS/NS-pG) composite for SCs in which 3D CCS microspheres distributed ultra-orderly on NS-pG sheets. CCS microspheres are formed through the nucleation and growth mechanism on the surface of NS-pG sheets. For better comparison, we also prepared CCS, CCS/pG to investigate the synthesis mechanism and also their respective supercapacitive performances. This work obviously shows the significant importance of porosity into the graphene frameworks as well as morphology-tuned structures, which were confirmed by enhanced electrochemical performance of the electrode. To the best of our knowledge, capacitance and energy density obtained in this study for the hybrid structure of CuCo₂S₄ and graphene-based material are the best among the reported results until now.

2. Experimental section

2.1. Material preparation

2.1.1. Synthesis of pG

All chemicals in this study were of analytical grade and they were directly used without further purification. Graphene oxide (GO) was prepared from graphite powders (Alfa Aesar, natural, -100 mesh, 99.995%) through the oxidation process using the modified hummers' method (Pham et al., 2013). Porous graphene oxide (pG) was synthesized by hydrothermal reduction of GO sheets using H₂O₂ (30%). Briefly, GO (50 mL, 2 mg mL⁻¹) was exfoliated in deionized (DI) water with continuous ultrasonication for 2 h to give a homogeneous aqueous dispersion. Next, 500 μ L of H₂O₂ (30%) solution was added to the graphene oxide dispersion, followed by gentle stirring for 30 min. Finally, the mixture was transferred to a Teflon-lined autoclave and was treated at 180 °C for 6 h. After being cooled to room temperature naturally, the resultant pG hydrogel was washed with DI water several times to remove the impurities and dried at 50 °C in vacuum oven for 12 h (Tang et al., 2015).

2.1.2. Synthesis of NS-pG

NS-pG was prepared through the one-pot hydrothermal method. First, pG (50 mL, 2 mg mL⁻¹) was dispersed in the ultrasonic bath for 2 h. Then, 1 g of thiourea (Sigma Aldrich, ACS reagent, \geq 99.0%) was added to the solution, followed by stirring for 2 h. After that, the mixture was transferred into a 100 mL Teflon-lined autoclave and thermally treated at 200 °C for 12 h. After cooling down to room temperature, the precipitate was collected and washed with DI water and ethanol several times. Finally, the product was dried at 50 °C for 24 h in a vacuum oven.

2.1.3. Synthesis of hybrid CCS/NS-pG composite

To synthesize hybrid CCS/NS-pG composite, pG (50 mL, 2 mg mL⁻¹) was firstly dispersed in the mixture of DI water and absolute ethanol (DI: Et; 3:7% v/v) under ultrasonication for 2 h. Then, the obtained dispersion solution was mixed gently with 2.0 mmol of copper nitrate trihydrate (Sigma Aldrich, puriss. p.a.,

99%–104%) and 4.0 mmol of cobalt nitrate hexahydrate (Sigma Aldrich, ACS reagent, $\geq 98.0\%$) under magnetic stirring for 1 h. Subsequently, 10.0 mmol of $\text{Na}_2\text{S} \cdot 9\text{H}_2\text{O}$ (Sigma Aldrich, ACS reagent, $\geq 98.0\%$) was added to dispersion system. After stirring for 1 h, the mixture was transferred to the Teflon-lined stainless-steel autoclave and was cured at 200°C for 24 h. For comparison, CCS microspheres were synthesized using the similar approach at temperatures of 160° , 180° and 200° but without the addition of NS-pG. Moreover, CCS/pG was prepared through the same method using undoped pG.

2.2. Material characterization

The crystal structure of the samples was investigated using the D8 ADVANCE ECO in a 1 kW copper X-ray tube diffractometer (XRD) with the scan range of 10 to 90 degrees (2θ). The morphology and chemical compositions of the as-prepared materials were observed by scanning electron microscope (FESEM, Jeol JSM-7400F) along with energy-dispersive X-ray spectrometer (EDX). The surface electron state of the samples was determined by X-ray photoelectron spectroscopy (XPS, Kratos Axix ultra DLD). The FTIR spectra of the samples were recorded using the Thermo Scientific Nicolet iS5 in the range of 4000 and 400 nm^{-1} . Brunauer-Emmett-Teller (BET) model (Micromeritics Tristar 3000, at 77 K) was used to measure the specific surface area. Pore size distribution of the sample was obtained from the desorption branch of the nitrogen isotherm through the Barrett-Joyner-Halenda (BJH) model. Raman scattering spectra were obtained using a Raman spectrometer with 632 nm excitation (Labram-010, France).

2.3. Electrochemical measurements

The electrochemical performance of CCS, CCS/pG, and CCS/NS-pG samples were studied using SP-150 electrochemical workstation (Biologic Science Instruments) through the three-electrode electrochemical method. The electrochemical setup was comprised of Pt as the counter electrode, Ag/AgCl electrode as the reference electrode, and as-prepared samples as the working electrode, in a 2 M KOH as the electrolyte. The working electrodes were fabricated by mixing the active material (85% in mass), AC as the conductive agent (10% in mass) and polyvinylidene fluoride as binder (PVDF) (5% in mass) in N-methyl-2-pyrrolidinone (NMP) solvent to form a slurry paste. Then the prepared paste was coated on the Ni foam ($2 \times 1\text{ cm}$) as the current collector and was placed in the vacuum oven at 80°C for 12 h to evaporate the solvent. The total mass value for all working electrodes were about 2 mg after drying. Cyclic voltammetry (CV) and Galvanostatic charge-discharge (GCD) methods were employed to study the charge storage capabilities and stability performance of the samples. The potential range of 0 to 0.5 V , along with different scan rates (5 , 10 , 20 , 50 and 70 mV s^{-1}), were performed for CV measurement. Similarly, for GCD measurement, different current densities (1 , 2 , 5 , 10 , 15 A g^{-1}) were recorded. Also, the electrochemical impedance spectroscopy (EIS) was carried out in the frequency range of 100 Hz to 100 kHz . The specific electrode capacity was calculated from the following equation: (Isacfranklin et al., 2021)

$$C_m = \frac{I \times \Delta t}{m \times \Delta V} (\text{F g}^{-1}) \quad (1)$$

Where I is discharge current (A), Δt is discharge time (s), m is total loaded mass of active material (mg) and ΔV is working potential window (V). The specific capacitance, can also be expressed in C g^{-1} or mA h g^{-1} according to the following formulas: (Isacfranklin et al., 2021)

Specific capacitance from CV plot: C

$$= \frac{\int I \times dv}{2 \times 3.6 \times m \times v} (\text{mA h g}^{-1}) \quad (2)$$

$$\text{Specific capacitance from GCD plot: } C = \frac{I \times \Delta t}{3.6 \times m} (\text{mA h g}^{-1}) \quad (3)$$

Where $I \times dv$ is CV curve area, I is discharge current (A), Δt is discharge time (s), m is total mass of active material (mg), and v is scan rate (mV s^{-1}).

2.3.1. Assembly of asymmetric supercapacitor device (ASC)

In two-electrode setup, the device was fabricated by employing the CCS/NS-pG nanohybrid as the positive electrode and AC as the negative electrode in 2 M KOH as an electrolyte in which the two electrodes were separated by cellulose paper. To obtain the highest performance of ASC device, the optimal mass ratio (m_+/m_-) of the positive/negative electrodes was calculated according to charge-balance theory using the following equation:

$$\frac{m_+}{m_-} = \frac{C_- \times \Delta V_+}{C_+ \times \Delta V_-} \quad (4)$$

The energy density (E) and power density (P) of the solid-state electrode device were then calculated according to equation number (5) and (6), respectively: (Li et al., 2020; Guan et al., 2020)

$$E = \frac{C \times \Delta V^2}{7.2} (\text{W h kg}^{-1}) \quad (5)$$

$$P = \frac{3600 \times E}{\Delta t} (\text{W kg}^{-1}) \quad (6)$$

where E is specific energy (W h kg^{-1}), C is specific capacitance of solid-state device (F g^{-1}), ΔV is working potential window (V), P is power density (W kg^{-1}), and Δt is discharge time (s).

3. Results and discussion

3.1. Growth mechanism

To better understand the synthesis and growth mechanism, we employed three temperature sets, including 160° , 180° , and 200° while all other parameters were constant in three experiments, to track the changes on the CCS microspheres morphology. The obtained FESEM images illustrated in Fig. 1a,b and c confirm that CCS microspheres were formed through the cluster-aggregative pathway (Takesue et al., 2011; You and Fang, 2016). According to this theory, it can be suggested that there are three distinct periods involved in the forming of CCS microspheres. In the first period, Cu^{2+} and Co^{2+} metal ions are reduced to Cu^0 and Co^0 atoms. Then, in second period which is the nucleation stage, CCS clusters are actively produced and then through the agglomeration of the clusters, CCS particles were formed (Fig. 1a). During the nucleation and seed formation period, CCS clusters are completely consumed. The last stage named as particle growth occurs by coalescence and aggregation of smaller CCS nanospheres, leading to larger CCS microspheres which are smooth on their surface (Fig. 1b and c). This process is extensively depicted in Scheme 1.

The growth mechanism proposed in Scheme 1 after observing some microspheres with negligible bumps on their outer shell in the FESEM images of CCS samples prepared at 200° . To clarify the mechanism, two other sets of experiments were carried out while the temperature was considered as the only changeable parameter. From the images of the microspheres at 160° , only small, aggregated particles are observed. But by increasing the temperature, it can be seen the size of the particles grew larger

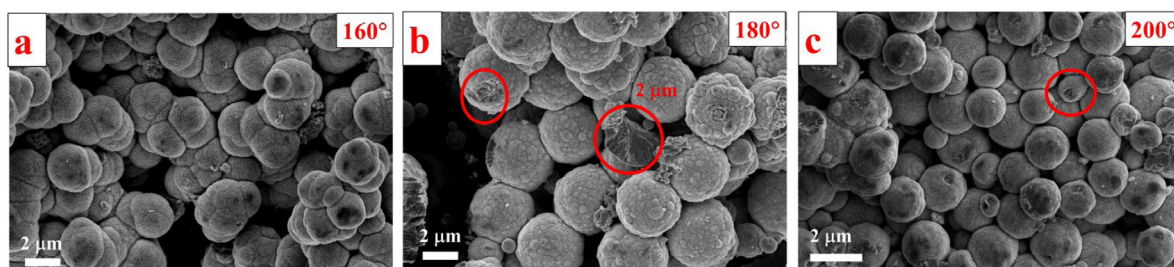
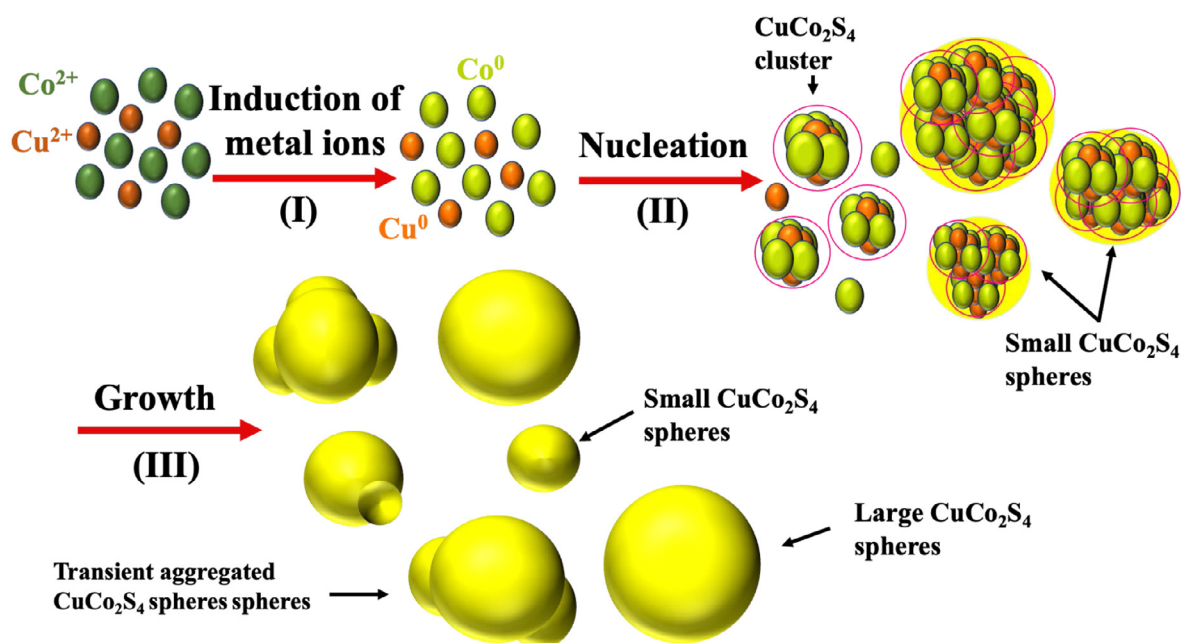


Fig. 1. FESEM images of CCS microspheres at 160° (a); FESEM image of CCS microspheres at 180° (b); FESEM image of CCS microspheres at 200° (c).



Scheme 1. Proposed mechanism of CCS microspheres formation; in stage one, the metal ions are reduced to metal atoms. Then CCS clusters were nucleated and simultaneously consumed in CCS particles formation. In the last step, the created small particles, grew to larger CCS microspheres through the coalescence and aggregation process.

and bumps nearly disappeared from the surface, which confirms the particle growing mechanism stages. It is noteworthy to mention that the areas of the microspheres which marked with red circles, are indicating that these microspheres are not hollow inside and this strengthens our growth mechanism suggestion.

Based on this mechanism, it can be also claimed that in hybrid CCS/NS-pG composite, the seed and nuclei were formed on the surface of graphene sheets and then through the particle growth process they grew to larger particles and formed a very uniform decorated structure in which the graphene sheets garnished with well-shaped CCS microspheres.

3.2. Morphological and structural characterization

The pG was synthesized by hydrothermally reducing GO using the H_2O_2 (Xu et al., 2014). During the hydrothermal process, the reduced graphene oxide (rGO) sheets with recovered strong p-p and vdW interactions, self-assemble into the pG hydrogel with interconnected 3D porous framework, and at the same time, H_2O_2 through the partial oxidizing and preferential etching of defective sites of GO, produces in-plane vacancies, which gradually extend to nanopores (Xu et al., 2014). In the next step, by addition of thiourea as the dopant agent, N and S elements were doped into the pG hydrogel. Inset of Fig. 2a shows the images of pG and NS-pG hydrogels. As it is clear from the images, the size of NS-pG hydrogel is bigger than the pG hydrogel suggesting that the

NS-pG is richer in porosity which led to volume expansion of hydrogel. Our experiment also showed by increasing the quantity of H_2O_2 during the synthesis process, the interconnected 3D framework gradually got destroyed and for quantity more than 1 mL of H_2O_2 , the whole pG was oxidized/dissolved and only a clear solution left.

To further reveal the microstructure of products, FESEM analysis was carried out. Images of NS-pG confirmed that this hydrogel was formed of uniform interconnected 3D hierarchical structure with abundant pores (Fig. 2a and b). It has been reported that when graphene sheets with 3D porous network structure is employed as the electrode in SCs, adsorption and diffusion of ions from the electrolyte is accelerated, and accordingly, the electrochemical performance will enhance (Wang et al., 2015). The different FESEM images of 3D hierarchical CCS microspheres with average diameter of $2.6 \mu\text{m}$ in the absence of NS-pG sheets, confirmed that microspheres has been formed through the nucleation and growth stages as illustrated in Fig. 2(c–g) (Zheng et al., 2014). This mechanism is also confirmed by microspheres that have noticeable bumps on their outer shell as shown on Fig. 2c (pointed microsphere), and 2d. Furthermore, as it is mentioned in previous section, the broken particles in the images suggesting that the microspheres are not hollow inside (Fig. 2e and f).

FESEM images of CCS/NS-pG hybrid sample is depicted in Fig. 2h and i. As shown in the image, 3D hierarchical CCS microspheres were uniformly and neatly distributed on the surface

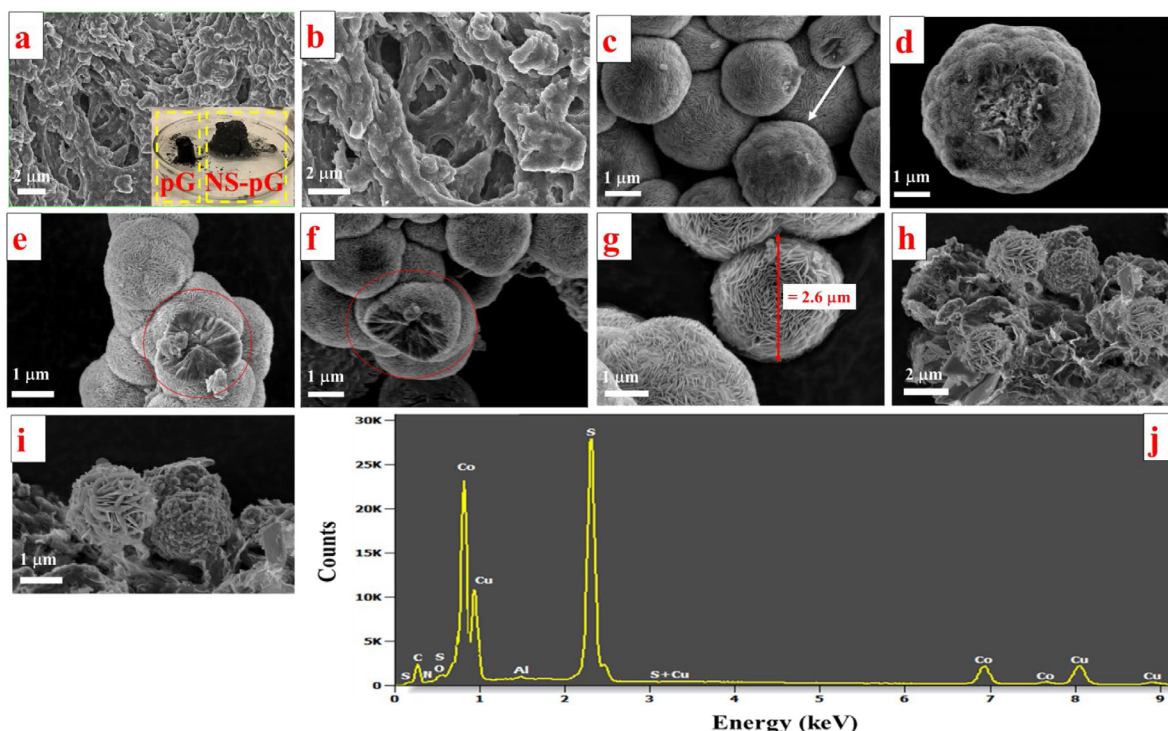


Fig. 2. FESEM image of NS-pG sheets and inset represents the photographs of as-prepared pG and NS-pG hydrogels (a); FESEM image of NS-pG with higher resolution (b); FESEM images of CCS microspheres prepared at 200° (c and d); FESEM images of CCS microspheres prepared at 160° (e and f); FESEM images of hybrid CCS/NS-pG composite (h and i); EDX pattern of hybrid CCS/NS-pG composite (j).

of NS-pG sheets without aggregation. Furthermore, addition of NS-pG sheets in the preparation process did not affect the morphology of the CCS, and NS-pG sheets were orderly decorated by CCS microspheres. Moreover, combining the wrinkled and holey texture of NS-pG sheets with rough and highly porous CCS microspheres results in an intimate contact between CCS and NS-pG sheets, which brings about advantages such as high specific surface area and facilitated charge transfer (Kaverlavani et al., 2017). EDX spectrum of hierarchical CCS/NS-pG hybrid obviously shows the presence of N, S, Cu, Co and C atoms. The Cu: Co: S atomic ratio was detected to be about 1:2:4, which is in good agreement with formation of stoichiometric ratio of CCS.

To investigate the structural and crystalline properties of the samples, XRD analysis was performed (Fig. 3a). GO, pG, NS-pG shows diffraction peaks at 2θ values of 11.8° , 23.7° and 24.3° respectively. The observed broad peaks of pG and NS-pG is due to the residual amount of water which is confined in the framework of these two samples, and also poor ordering of graphene sheets after reduction as reported elsewhere (Kong et al., 2016). Regarding the CCS microspheres, the observed peaks can be successively indexed to (111), (220), (311), (400), (422), (511) and (440) crystal facets which represent the cubic structure of CuCo_2S_4 (PDF# 42-1450) (Wu et al., 2020). However, the attributed peak of NS-pG at 24.3° is not obvious in CCS/NS-pG XRD pattern which may be due to the uniform coverage of CCS microspheres on NS-pG sheets as well as low amount of NS-pG component (25%) in the whole hybrid structure.

Fig. 3b shows Raman spectra of the prepared GO, pG, NS-pG, CCS and CCS/NS-pG samples. It can be seen by modification of GO to pG and NS-pG, the intensity ratio of I_D/I_G gently increased from 0.94 to 1.14 and 1.21, respectively. The higher values of I_D/I_G in pG and NS-pG indicate significant number of in-plane pores, which are rich in edge-defects in 2D graphene sheets. Furthermore, it reveals that GO had been reduced through the hydrothermal process. In case of CCS and CCS/NS-pG, two distinct peaks at 512 and 689 cm^{-1} can be observed in the Raman

spectra, which are characteristic of CCS microspheres (Wu et al., 2020). Also, in CCS/NS-pG spectra, the two sharp peaks of D-band (1357 cm^{-1}) and G-band (1601 cm^{-1}) attributed to NS-pG confirm the successful combination of CCS and NS-pG.

3.3. Composition and surface elements characterization

FTIR and XPS were performed to investigate the surface elemental composition and chemical states. In Fig. 4 the FTIR spectra of GO, pG and NS-pG structures, are depicted. In GO spectra, five characteristic peaks at 3351 , 1730 , 1615 , 1246 , 1073 cm^{-1} were identified as stretching vibration of O-H, C=O, C=C, C-O-C and C-O, respectively, indicating the oxygen-functional groups were introduced into the Graphite structure after modified hummers' reaction. Notably, after modification of GO with H_2O_2 and thiourea through the hydrothermal process, most of the oxygenated functional groups reduced, followed by introducing of N (1440 cm^{-1}) and S (1193 cm^{-1}) to the structure of graphene sheets (Periyasamy et al., 2021).

The surface electronic state and element composition of hybrid CCS/NS-pG composite were investigated by XPS as exhibited in Fig. 5 (a-f). In Fig. 5 (b-f), the high-resolution XPS spectra of Cu 2p, Co 2p, S 2p, N 1s and C 1s are illustrated. The spectra of Cu 2p are formed by peaks of $2p_{1/2}$ (952.09 eV) and $2p_{3/2}$ (932.28 eV) along with two satellite peaks (Mehare et al., 2018). The XPS spectra of Co 2p are deconvoluted into two separate peaks of Co^{2+} positioned in 780.53 eV , 796.32 eV and Co^{3+} characterized at 778.65 eV and 793.55 eV , respectively (Mehare et al., 2018). The S 2p spectrum also shows one satellite peak positioned at 168.52 eV along with three more peaks. The peaks centered at 161.26 eV and 162.64 eV are characteristics of S $2p_{3/2}$ and S $2p_{1/2}$, respectively. Besides, the peak positioned at 164.01 eV could be ascribed to sulfur-metal (S-M) bond (Mehare et al., 2018). N 1s XPS spectra are deconvoluted into three distinct peaks including pyridine-N, pyrrole-N, and graphite-N confirming that

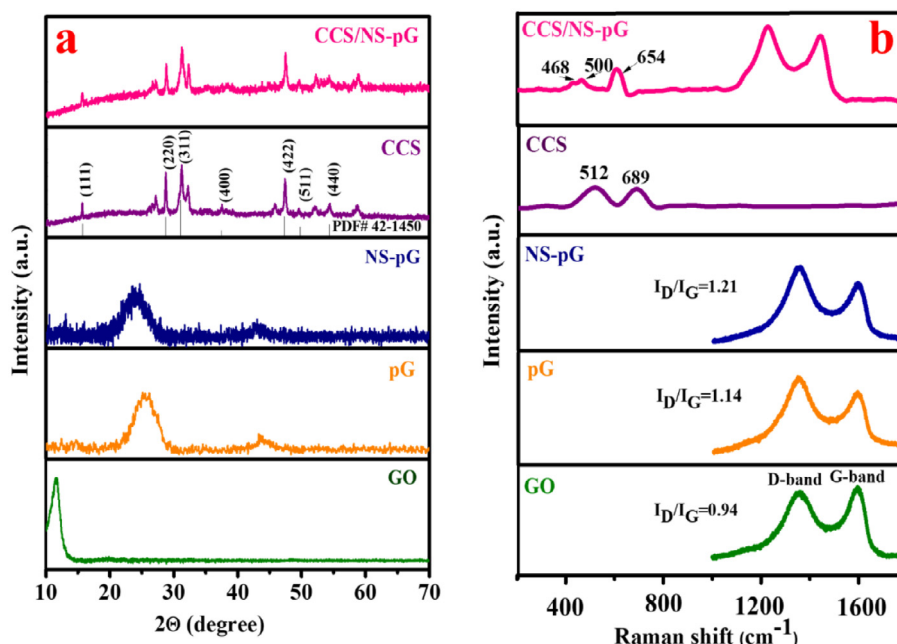


Fig. 3. XRD patterns of GO, pG, NS-pG, CCS and CCS/NS-pG (a); Raman spectra of GO, pG, NS-pG, CCS and CCS/NS-pG (b).

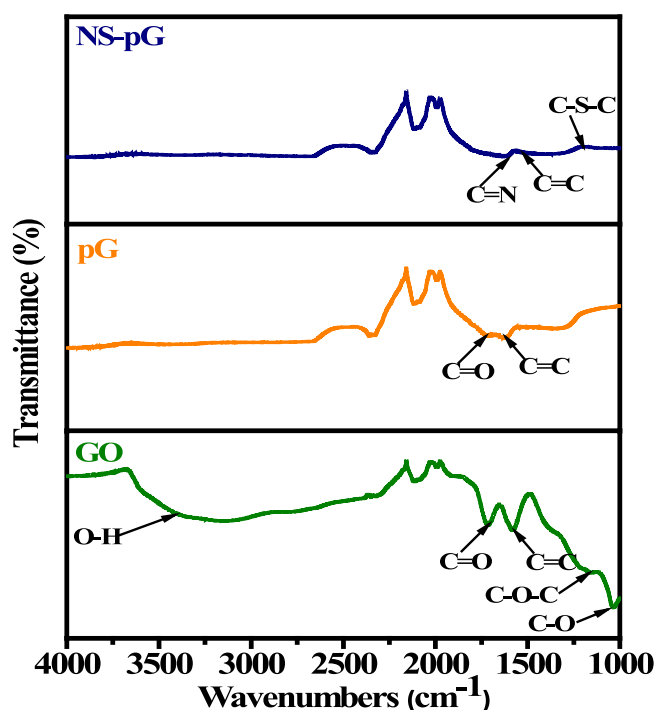


Fig. 4. FTIR spectra of GO, pG, NS-pG.

pG doped with nitrogen atoms (Mehare et al., 2018). Moreover, C1s spectrum showing four deconvoluted peaks corresponding to five different atoms including C-S (286.54 eV), C-N (285.76 eV), C-C/C = C (284.46 eV) and C=O (287.44 eV). The composition of hybrid CCS/NS-pG composite structure is then confirmed by the XPS result (Li et al., 2019).

3.4. Surface area analysis

The specific surface area and pore size distribution of as-prepared CCS and CCS/NS-pG samples were investigated through

the BET and BJH measurement and the results are illustrated in the Fig. 6a. The N_2 adsorption-desorption isotherms with BJH studies (inset of Fig. 6a) reveals the typical type of IV isotherms which are accompanied by an evident hysteresis loop in both samples. Moreover, as illustrated in inset of Fig. 6a, there is a wide distribution of pore size in the range of 2–50 nm in both samples confirming that both samples contain mesopores in their structures. However, compared to CCS, the N_2 adsorption-desorption isotherm of hybrid CCS/NS-pG composite shows larger hysteresis loop in the P/P_0 range of 0.5 to 0.95, confirming the existences of rich mesopores in CCS/NS-pG structure.

This is verified by specific surface area of 40.6 and 101.4 $m^2 g^{-1}$ in CCS and CCS/NS-pG samples. The abundant pores in CCS/NS-pG structure due to the holey structure of graphene sheets not only can provide a greater number of active sites for electrochemical reactions but also decrease the charge transfer resistance (Wu et al., 2020). All aforementioned characterizations studies confirmed that the well-formed hybrid CCS/NS-pG composite structure could be employed as an efficient electrode in SCs.

3.5. Electrochemical performance of the electrodes

The electrochemical performance of the as-prepared electrodes was evaluated in a three-electrode setup in which 2 M KOH was utilized as the aqueous electrolyte. Fig. 7a shows the CV graphs of bare Ni foam, CCS, CCS/pG, and CCS/NS-pG at a scan rate of 5 $mV s^{-1}$, respectively. As evident in the graph, the CV integrated area increased gradually from bare Ni foam to CCS/NS-pG, meaning that the holey structure of graphene and co-doping of the graphene sheets with N and S atoms leads to a synergetic effect between CCS microspheres and NS-pG sheets. As a result, CCS/NS-pG-based electrode shows the highest response current compared to the other electrodes which results in improved capacity and higher energy density (Wu et al., 2020). Fig. 7b depicts the CV curves of CCS/NS-pG at different scan rates of 5, 10, 20, 50 and 70 $mV s^{-1}$. The obtained CV profile shows the distinct redox peaks in potential range of 0–0.5 V relates to faradaic reactions of $Co^{2+}/Co^{3+}/Co^{4+}$ and Cu^+/Cu^{2+} , verifying the pseudocapacitive behavior of the electrode. As seen, increasing the scan rate results

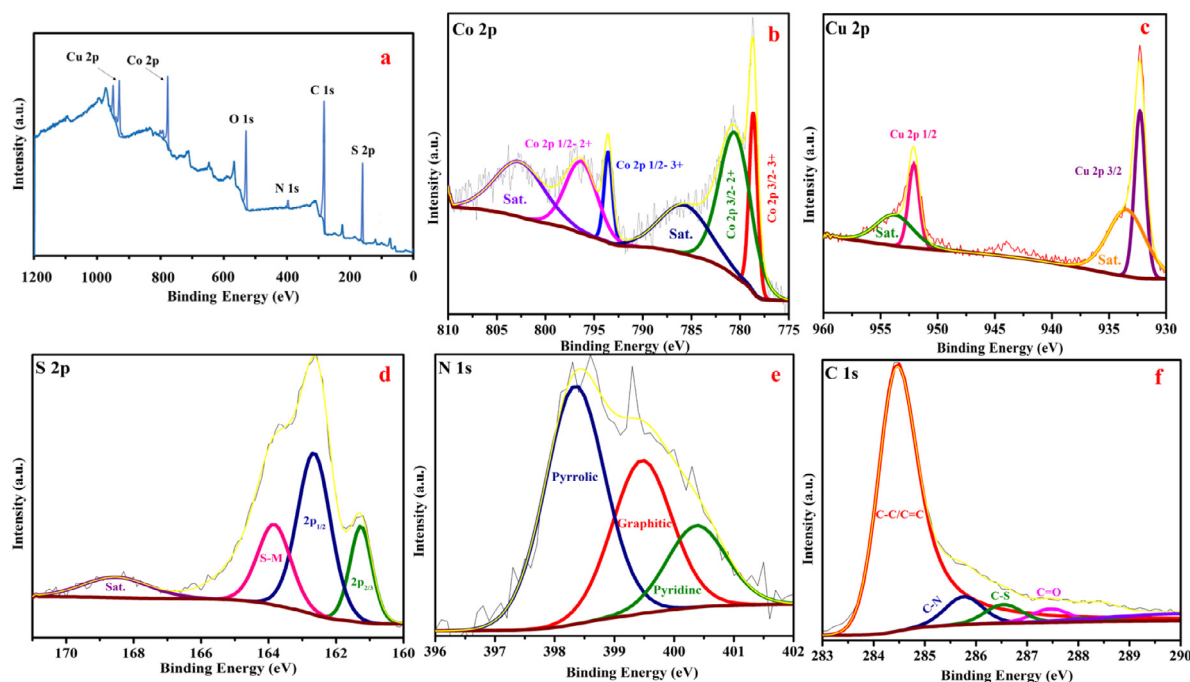


Fig. 5. Survey XPS spectrum of CCS/NS-pG (a); High-resolution XPS spectra of Co 2p, Cu 2p, S 2p, N 1s, and C 1s of the CCS/NS-pG sample (b-f).

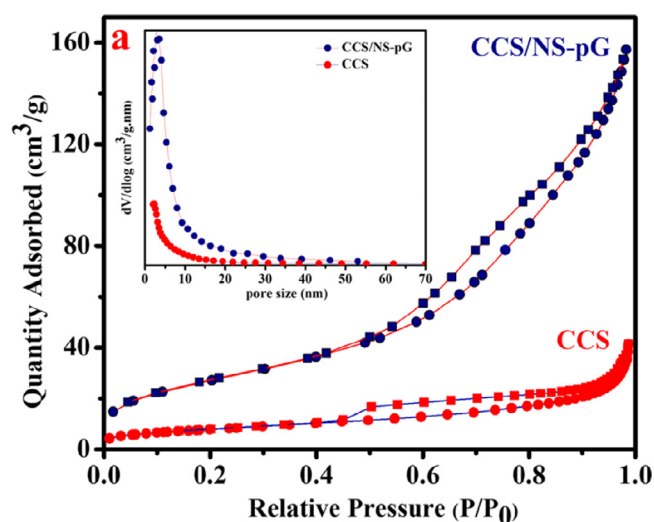


Fig. 6. N_2 adsorption-desorption isotherm loops of CCS and CCS/NS-pG samples and inset is the pore size distribution curves of CCS and CCS/NS-pG (a).

in larger integrated area of CV curves. Moreover, even at higher scan rates, the redox peaks are unchanged, suggesting a surface-controlled electrochemical reaction and facilitated electronic and ionic transport process (Zhou et al., 2015).

The GCD behavior of CCS, CCS/pG, and CCS/NS-pG electrodes were carried out to measure the specific capacitance, stability, and rate capability of the electrodes. Fig. 7c shows the GCD curves of CCS, CCS/pG, and CCS/NS-pG electrodes at 1 A g^{-1} . From the obtained GCD curves, the specific capacitance of CCS, CCS/pG, and CCS/NS-pG were calculated as 737.5, 1155.6, and 1357.8 A g^{-1} , respectively. As expected, CCS/NS-pG exhibited the highest specific capacitance compared to pure CCS and CCS/pG and other materials which were reported previously such as prGO (568.5 F g^{-1}) (Ma et al., 2021), porous graphene-NiO (PGNO) (511 F g^{-1}) (Sethi et al., 2021), NiCo_2S_4 @HGh (1000 F g^{-1}) (Tiruneh et al., 2018), Mn_3O_4 - CeO_2 /holey-graphene (568.5 F g^{-1}) (Qian et al., 2019), $\text{CuCo}_2\text{S}_4/\text{N}$, S-RGO nanosheets (644 F g^{-1}) (Li et al., 2019), CuCo_2S_4 -rGO composite (1141.64 F g^{-1}) (Wu et al., 2020), CoNi_2S_4 nanosheets into S, P co-doped graphene (DGNCS) (1136.5 F g^{-1}) (Jing et al., 2020). The outstanding electrochemical performance of CCS/NS-pG electrode attributes to the larger active sites provided by pG sheets, ultra-ordered decoration of CCS microspheres which impede the aggregation of graphene sheets and shortening of diffusion path for electrolyte ions (Li et al., 2019).

Fig. 7d shows GCD curves of CCS/NS-pG electrode at various current densities ranging from 1 to 15 A g^{-1} . The distortion of GCD curves caused by the faradaic character of the electrode indicate the battery-type behavior. The specific capacitance of CCS/NS-pG, CCS/pG and CCS-based electrodes at different current densities are illustrated in Fig. 7e. As clearly seen, CCS/NS-pG electrode presents a relatively long discharge time at all evaluated current densities with specific capacitance of 1357.8, 1191.2, 855.6, 600 and 333.4 F g^{-1} at the respective current densities of 1, 2, 5, 10, 15 A g^{-1} , respectively. Furthermore, by increasing the current density to 10 A g^{-1} , 95.9% of the initial capacitance was retained after 5000 cycles (Fig. 7f). As illustrated in the insets of Fig. 7f, in order to verify the stability of charge-discharge curves in first and last cycles reveals the high columbic efficiency and minimum polarization of electrode's material (Zhou et al., 2015). The Nyquist plots of the CCS, CCS/pG, and CCS/NS-pG electrodes are displayed in Fig. 7g. The larger slope in low frequencies, the absence of semicircle in high frequencies, and very low R_{ESR} verify the fast ion diffusion and low charge transfer resistance for the CCS/NS-pG electrode compared to the other electrodes.

3.6. Electrochemical performance of CCS/NS-pG//AC asymmetric supercapacitor device (ASC)

To further evaluate the CCS/NS-pG electrode for practical application, an asymmetric device by using CCS/NS-pG as the

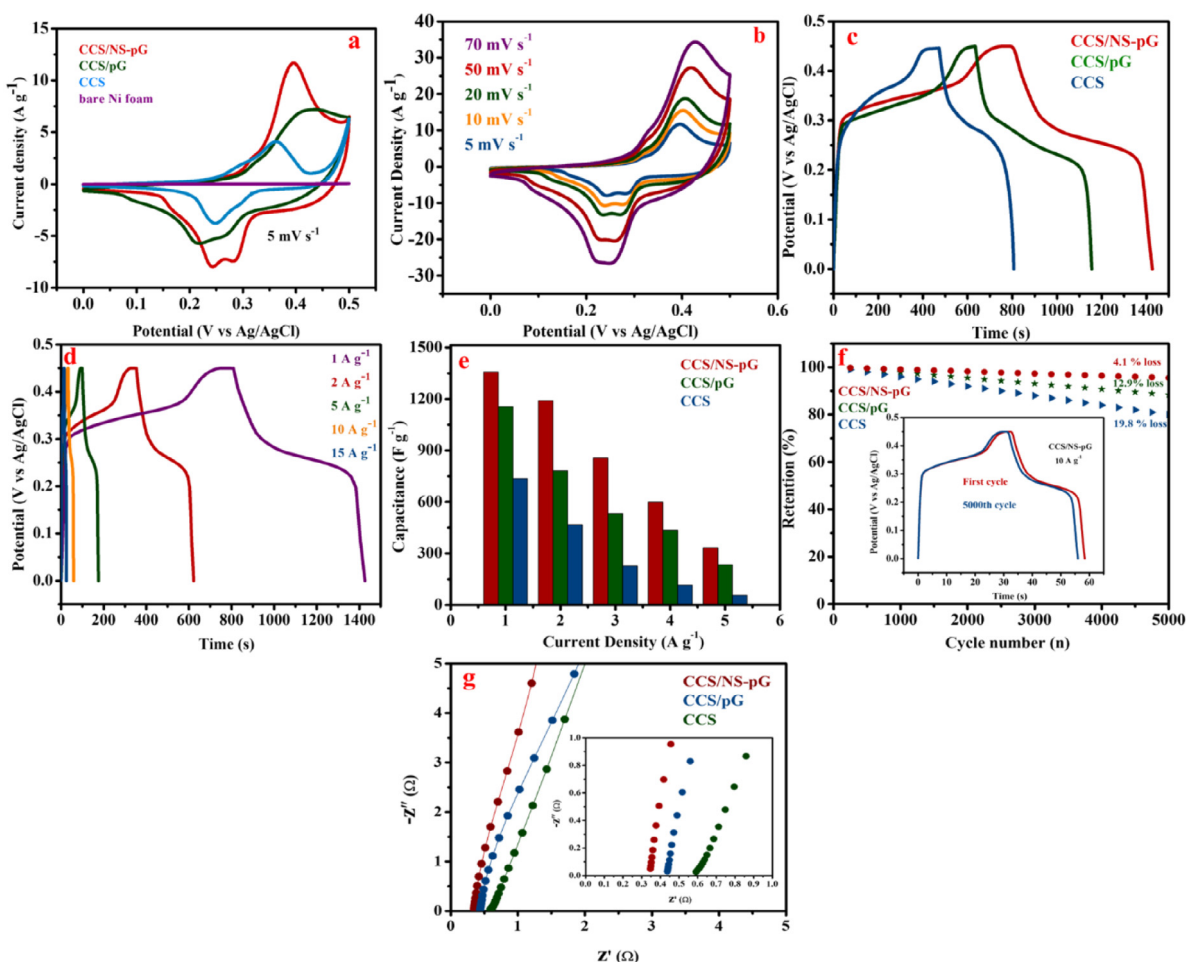


Fig. 7. Electrochemical characterizations of as-prepared electrodes in the three-electrodes setup: CV curves of the CCS, CCS/pG and CCS/NS-pG electrodes at the scan rate of 5 mV s^{-1} in aqueous 2 M KOH electrolyte (a); CV curves of CCS/NS-pG electrode at different scan rates (b); GCD curves of the CCS, CCS/pG and CCS/NS-pG electrodes at the current density of 1 A g^{-1} (c); GCD curves of the CCS/NS-pG electrode at different current densities (d); Specific capacitance of CCS, CCS/pG and CCS/NS-pG electrodes (e); Cycling performance of CCS, CCS/pG and CCS/NS-pG electrodes (f); Nyquist plots of CCS, CCS/pG and CCS/NS-pG electrodes, and the inset is the expanded high-frequency region (g).

cathode and AC as the anode in which the two electrodes were separated by cellulosic paper while using the 2 M KOH as the electrolyte, was fabricated. There are two advantages with this configuration: (i) employing the AC as the EDLC negative electrode accompanying with positive electrode would increase the specific capacitance of the device through the redox reactions on positive electrode surface and (ii) because of high overpotential causing by reversible hydrogen electroadsorption on EDLC electrode surface, the potential window will expand resulting in higher energy density (Kaverlavani et al., 2017). Fig. 8a shows the CV curves of AC and CCS/NS-pG electrode at 20 mV s^{-1} after mass balance as in Eq. (4). The AC electrode shows the typical property of EDLC materials ranging from -1 to 0 V while the positive CCS/NS-pG electrode exhibits working voltage within the range of 0 to 0.5 V . Fig. 8b represents the CV curves of ASC device at different potential window at scan rate of 70 mV s^{-1} . As seen, more expansive potential windows lead to higher electrochemical polarization, which is evident as the sharp peaks at 1.8 and 2 V . Based on the CV and GCD evaluation of the device, the potential window of 1.6 V as the ideal voltage window was chosen. CV curves of the ASC device were recorded at various scan rates of $5, 10, 20, 50,$ and 70 mV s^{-1} (Fig. 8c). As shown,

ASC device reveals both battery-type and electric double layer behavior. Furthermore, all CV curves exhibit a perfect identical shape indicating significant rate capability and reversibility of the device (Kaverlavani et al., 2017). GCD evaluation at different current densities, further confirmed the significant capacitive behavior of the device accomplished by shared advantages from both EDLC and pseudocapacitance electrodes. (Kaverlavani et al., 2017) The GCD curves show no internal voltage drop verifying the high-rate capability of the device (Fig. 8d). The calculated specific capacitance of ACS is $226.8, 204.5, 177.4,$ and 153.9 F g^{-1} at current densities of $1, 2, 5$ and 10 A g^{-1} , respectively. The maximum specific capacitance of 226.8 F g^{-1} at current density of 1 A g^{-1} is comparable with other ASC devices reported recently as presented in Table 1. For better comparison, we not only include the recently reported works combined composite material of CuCo_2S_4 and graphene, but also, we present composites which contains other binary metal sulfides and graphene for supercapacitor application. The ASC device is shown to deliver an excellent maximum energy density of $80.59 \text{ W h kg}^{-1}$ at a power density of $2302.65 \text{ W kg}^{-1}$. Notably, the energy density remained still at $55.31 \text{ W h kg}^{-1}$ when the power density increased to

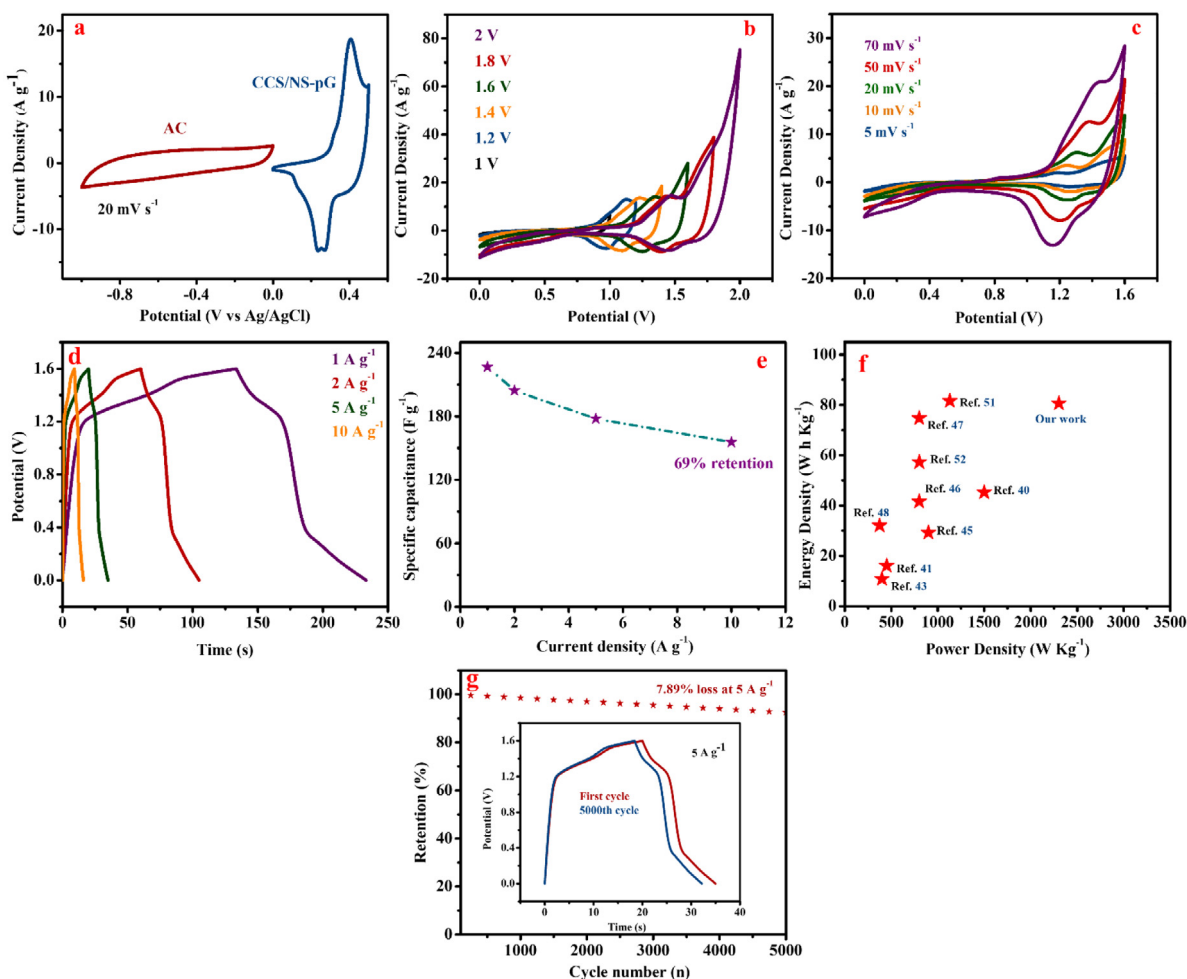


Fig. 8. Electrochemical studies of CCS/NS-pG//AC asymmetric device: CV curves of AC and CCS/NS-pG electrodes at the scan rate of 20 mV s^{-1} in aqueous 2 M KOH electrolyte in a half-cell setup (a); CV curves of CCS/NS-pG//AC asymmetric device at different potential windows (b); CV curves of CCS/NS-pG//AC asymmetric device at different scan rates (c); GCD curves of the CCS/NS-pG//AC asymmetric device at different current densities (d); rate capability of the device (e); Comparison between Ragone plot of CCS/NS-pG//AC asymmetric device and other previously reported works (f); Cycling performance of CCS/NS-pG//AC asymmetric device (g).

$10479.53 \text{ W kg}^{-1}$ showing the device can retain 69% of initial capacitance after increasing the current density from 1 to 10 A g^{-1} as shown in Fig. 8e. Corresponding Ragone plot of energy and power density, depicted in Fig. 8f, evidently demonstrates the enhanced performance of CCS/NS-pG//AC asymmetric supercapacitor device compared to previously reported works. As presented in table 1, our device showed a maximum energy density of $80.59 \text{ W h kg}^{-1}$ at a power density of $2302.65 \text{ W kg}^{-1}$, which is much higher than recently fabricated symmetric devices (SCS) such as $\text{CuCo}_2\text{S}_4\text{-rGO//CuCo}_2\text{S}_4\text{-rGO}$ ($16.07 \text{ W h kg}^{-1}$) (Wu et al., 2020), and also higher than reported asymmetric devices including $\text{CuCo}_2\text{S}_4/\text{N, S-RGO//N, S-RGO}$ (10.8 W h kg^{-1}) (Li et al., 2019). Moreover, the fabricated CCS/NS-pG//AC asymmetric device, showed a capacitance retention rate of 92.1% after 5000 cycles at current density of 5 A g^{-1} as exhibited in Fig. 8g. Comparison of the first and the 5000th cycle, indicates the stability and reversibility of the electrode. The significant electrochemical performance of CCS/NS-pG electrode can be attributed to the porous structure of graphene sheets accompanied by co-doping of N and S heteroatoms, which provide more available faradaic active sites through the penetration of the electrolyte into the inner surfaces, and also improved synergetic effects between CCS microspheres and NS-pG sheets in whole hybrid CCS/NS-pG composite structure.

4. Conclusion

Through the facile multi-steps hydrothermal and solvothermal approaches, we have developed a novel ultra-ordered hybrid $\text{CuCo}_2\text{S}_4/\text{NS-pG}$ composite-based electrode with significant high surface area with excellent synergetic performance for high-efficient asymmetric supercapacitors. We have focused beyond binary CuCo_2S_4 integrated graphene layers reported in the literature, and first developed highly mesoporous graphene structure, and incorporated nitrogen(N) and sulfur(S) into the graphene (NS-pG) framework in order to enhance the electrochemical performance of the CuCo_2S_4 based electrode. Employing controllable synthesis routes, which were dominated by nucleation and growth mechanism, we could attain a highly ordered array of CuCo_2S_4 microspheres on the surface of graphene sheets that were confirmed by FESEM images. Due to its unique structural and compositional properties, the hybrid sample showed remarkable capacitive performance as an electrode with 1357.8 F g^{-1} at current density of 1 A g^{-1} . Furthermore, the as-prepared asymmetric supercapacitor exhibited an outstanding energy density of $80.59 \text{ W h kg}^{-1}$ at a power density of $2302.65 \text{ W kg}^{-1}$ with superior cycle performance of 92.1% after 5000 cycles, which are the best results reported so far for this combined CCS/NS-pG hybrid material. The obtained results confirm that CCS/NS-pG hybrid-based electrode is a highly promising candidate for high-efficient energy storage devices.

Table 1
Summary of electrochemical performance of previously reported works compared to this work.

Material	Specific surface Area ($\text{m}^2 \text{g}^{-1}$)	Three electrode setup		Synthesis method	Two electrode setup		E (W h Kg^{-1})	P (W Kg^{-1})	Ref.
		Specific capacitance at current density	Cycle retention		Specific capacitance at current density	Cycle retention			
CuCo ₂ S ₄ -rGO composite	116.4	1141.64 F g ⁻¹ at 1.5 A g ⁻¹	84.03% @3000	hydrothermal	142.89 F g ⁻¹ at 1 A g ⁻¹	78.64% @3000	16.07	450	Wu et al. (2020)
Heterostructured SnCoO ₃ /rGO composite	13.782	30.80 mAh g ⁻¹	86.95% @5000	hydrothermal	166 F g ⁻¹ at 1 A g ⁻¹	74.28% @15000	52	752	Isacfranklin et al. (2021)
CuCo ₂ S ₄ /N, S-RGO nanosheets	52.7	644 F g ⁻¹ at 1 A g ⁻¹ 743 C g ⁻¹ at 1 A g ⁻¹	76.4% @5000	hydrothermal	30.5 F g ⁻¹ at 1 A g ⁻¹ 64.9 F g ⁻¹ at 1 A g ⁻¹	88.9% @5000	10.8	400	Li et al. (2019)
CoS ₂ @Ni(OH) ₂ core-shell nanotube	–	1813 F g ⁻¹ at 2 A g ⁻¹	91.6% @3000	electrochemical deposition process	144.6 F g ⁻¹ at 2 A g ⁻¹	85.5% @3000	29.22	899.2	Luo et al. (2020)
GW-CuCo ₂ O ₄ hollow spheres	106.2	1813 F g ⁻¹ at 2 A g ⁻¹	96.8% @6000	self-templated method	208 F g ⁻¹ at 1.4 A g ⁻¹	95.2% @6000	45.2	1500	Kaverlavani et al. (2017)
hybrid rGO-NiCo ₂ S ₄ composites	–	972 F g ⁻¹ at 1 A g ⁻¹	–	hydrothermal	117 F g ⁻¹ at 1 A g ⁻¹	94.1% @2000	56.62	701.37	Kumar et al. (2021)
NiCo ₂ S ₄ Nanoparticles/Carbon Nanotube	–	1110 F g ⁻¹ at 1 A g ⁻¹	87% @5000	solvothelmal	103.5 F g ⁻¹ at 1 A g ⁻¹	82% @5000	41.6	800	Yang et al. (2021)
NiCo ₂ O ₄ @NiCoAl-LDH	–	1814.2 F g ⁻¹ at 1 A g ⁻¹	93% @2000	Chemical bath deposition	104 F g ⁻¹ at 3 A g ⁻¹	99.5% @10000	74.7	800	He et al. (2017)
NiCo ₂ S ₄ @NiCo ₂ O ₄ core@shell nanoneedle/rGO	–	1590 F g ⁻¹ at 5 A g ⁻¹	96% @2000	hydrothermal	154 F g ⁻¹ at 1 A g ⁻¹	82% @1000	32	375	Singh et al. (2020)
CoNi ₂ S ₄ /rGO nanosheets	121.9	1526 F g ⁻¹ at 1 A g ⁻¹	–	one-step pyrolysis	72.06 F g ⁻¹ at 1 A g ⁻¹	93.7% @8000	54.8	798	Zhang et al. (2020)
CoNi ₂ S ₄ nanosheets into S, P co-doped graphene (DGNCS)	153.65	1136.5 F g ⁻¹ at 1 A g ⁻¹	70.1% @5000	multi-step hydrothermal	229.5 F g ⁻¹ at 1 A g ⁻¹	86.49% @5000	25.62	8000	Jing et al. (2020)
Y-doped α -Ni(OH) ₂ /graphene heterostructure	40.687	822.3 C g ⁻¹ at 1 A g ⁻¹	76.24% @2000	solvothelmal	74 F g ⁻¹ at 1 A g ⁻¹	83.28% @7000	81.6	1129.8	Zhu et al. (2020)
rGO- NiMoO ₄ @Ni-Co-S	–	318 mA h g ⁻¹	88.87% @10000	hydrothermal	24.6 F cm ⁻³ at 1 mA cm ⁻²	90.89% @10000	57.24	801.8	Acharya et al. (2021a)
3D MnO ₂ /HRGO composite	241.8	108.0 F cm ⁻³ at 1 mA cm ⁻²	72.2% @1000	hydrothermal	–	93.7% @1000	149.7 $\mu\text{Wh cm}^{-2}$	2.8 mWh cm ⁻³	Park et al. (2021)
Mn ₂ O ₄ -CeO ₂ /holey-graphene	160.21	310 F g ⁻¹ at 2 A g ⁻¹	92.4% @1000	hydrothermal	–	–	–	–	Qian et al. (2019)
NiCo ₂ S ₄ @HGH	–	1000 F g ⁻¹ at 0.5 A g ⁻¹	96.6% @2100	Solvothelmal and hydrothermal	312.6 F g ⁻¹ at 6 A g ⁻¹	87% @5000	21.3	8400	Tiruneh et al. (2018)
NiCo ₂ S ₄ /N, S-HRGO composite	29.7	184.2 mAh g ⁻¹ at 1 A g ⁻¹	91.8% @2000	hydrothermal	86 at 5 mV s ⁻¹	87.5% @10000	35.4	15000	Liu et al. (2021)
porous graphene-NiO (PGNO)	87	511 F g ⁻¹ at 5 mV s ⁻¹	80% @10000	solvothelmal	–	84% @10000	5.9	2000	Sethi et al. (2021)
prGO	18.7	568.5 F g ⁻¹ at 1 A g ⁻¹	126.4% @10000	one-pot microwave-assisted	434.8 F g ⁻¹ at 1 A g ⁻¹	–	15	2500	Ma et al. (2021)
Hybrid CuCo ₂ S ₄ /NS-pG composite	101.4	1402.22 F g ⁻¹ at 1 A g ⁻¹	95.9% @5000	hydrothermal	280.0 F g ⁻¹ at 1 A g ⁻¹	92.1% @5000	80.59	2302.65	This work

CRediT authorship contribution statement

Fatemeh Heidari Gourji: Conceptualization, Methodology, Data analysis, Writing the first draft. **Dhayan Velauthapillai:** Supervision, Review and edition, Validation. **Mansoureh Keykhaei:** Software, Resources.

Declaration of competing interest

The authors declare that they have no known competing financial interests or personal relationships that could have appeared to influence the work reported in this paper.

Data availability

No data was used for the research described in the article.

Acknowledgments

We gratefully acknowledge funding provided by Western Norway University of Applied Sciences (HVL) for UTFORSK and NORPART project with ID numbers UTF- 2021- long-term/10051 and NORPART-2021-10237. Also, The Research Council of Norway is acknowledged for the support to the Norwegian Micro- and Nano-Fabrication Facility, NorFab, project number 295864.

References

- Acharya, J., Ojha, G.P., Kim, B.-S., Pant, B., Park, M., 2021a. Modish designation of hollow-tubular rGO-NiMoO₄@ Ni-Co-S hybrid core-shell electrodes with multichannel superconductive pathways for high-performance asymmetric supercapacitors. *ACS Appl. Mater. Interfaces* 13, 17487–17500.
- Acharya, J., Park, M., Ko, T.H., Kim, B.-S., 2021b. Leaf-like integrated hierarchical NiCo₂O₄ nanorods@ Ni-Co-LDH nanosheets electrodes for high-rate asymmetric supercapacitors. *J. Alloys Compd.* 884, 161165.
- Amiri, M., Moosavifard, S.E., Davarani, S.S.H., Kaverlavani, S.K., Shamsipur, M., 2021. MnCoP hollow nanocubes as novel electrode material for asymmetric supercapacitors. *Chem. Eng. J.* 420, 129910.
- Arvas, M.B., Gürsu, H., Gencten, M., Sahin, Y., 2021. Preparation of different heteroatom doped graphene oxide based electrodes by electrochemical method and their supercapacitor applications. *J. Energy Storage* 35, 102328.
- Askari, M.B., Salarizadeh, P., Seifi, M., Rozati, S.M., Beheshti-Marnani, A., 2020. Binary mixed molybdenum cobalt sulfide nanosheets decorated on rGO as a high-performance supercapacitor electrode. *Nanotechnology* 31, 275406.
- Chen, W., Yuan, P., Guo, S., Gao, S., Wang, J., Li, M., Liu, F., Wang, J., Cheng, J., 2019. Formation of mixed metal sulfides of NiCu_{1-x}Co₂S₄ for high-performance supercapacitors. *J. Electroanal. Soc.* 836, 134–142.
- Chen, Z., Zhao, S., Zhao, H., Zou, Y., Yu, C., Zhong, W., 2021. Nitrogen-doped interpenetrating porous carbon/graphene networks for supercapacitor applications. *Chem. Eng. J.* 409, 127891.
- Coros, M., Varodi, C., Pogacean, F., Gal, E., Pruneanu, S.M., 2020. Nitrogen-doped graphene: The influence of doping level on the charge-transfer resistance and apparent heterogeneous electron transfer rate. *Sensors* 20, 1815.
- Geng, P., Zheng, S., Tang, H., Zhu, R., Zhang, L., Cao, S., Xue, H., Pang, H., 2018. Transition metal sulfides based on graphene for electrochemical energy storage. *Adv. Energy Mater.* 8, 1703259.

- Guan, S., Fu, X., Zhang, B., Lei, M., Peng, Z., 2020. Cation-exchange-assisted formation of NiS/SnS₂ porous nanowalls with ultrahigh energy density for battery-supercapacitor hybrid devices. *J. Mater. Chem. A* 8, 3300–3310.
- He, X., Liu, Q., Liu, J., Li, R., Zhang, H., Chen, R., Wang, J., 2017. Hierarchical NiCo₂O₄@NiCoAl-layered double hydroxide core/shell nanoforest arrays as advanced electrodes for high-performance asymmetric supercapacitors. *J. Alloys Compd.* 724, 130–138.
- Hooch Antink, W., Choi, Y., K.d. Seong, Kim, J.M., Piao, Y., 2018. Recent progress in porous graphene and reduced graphene oxide-based nanomaterials for electrochemical energy storage devices. *Adv. Mater. Interfaces* 5, 1701212.
- Isacfranklin, M., Yuvakkumar, R., Ravi, G., Hong, S., Velauthapillai, D., Thambidurai, M., Dang, C., Algarni, T.S., Al-Mohaimed, A.M., 2021. Heterostructured SmCoO₃/rGO composite for high-energy hybrid supercapacitors. *Carbon* 172, 613–623.
- Jing, C., Guo, X., Xia, L., Chen, Y., Wang, X., Liu, X., Dong, B., Dong, F., Li, S., Zhang, Y., 2020. Morphologically confined hybridization of tiny CoNi₂S₄ nanosheets into S, P co-doped graphene leading to enhanced pseudocapacitance and rate capability. *Chem. Eng. J.* 379, 122305.
- Kannan, A.G., Zhao, J., Jo, S.G., Kang, Y.S., Kim, D.-W., 2014. Nitrogen and sulfur co-doped graphene counter electrodes with synergistically enhanced performance for dye-sensitized solar cells. *J. Mater. Chem. A* 2, 12232–12239.
- Kaverlavani, S.K., Moosavifard, S., Bakouei, A., 2017. Designing graphene-wrapped nanoporous CuCo₂O₄ hollow spheres electrodes for high-performance asymmetric supercapacitors. *J. Mater. Chem. A* 5, 14301–14309.
- Kiciński, W., Szala, M., Bystrzejewski, M., 2014. Sulfur-doped porous carbons: Synthesis and applications. *Carbon* 68, 1–32.
- Kong, W., Duan, X., Ge, Y., Liu, H., Hu, J., Duan, X., 2016. Holey graphene hydrogel with in-plane pores for high-performance capacitive desalination. *Nano Res.* 9, 2458–2466.
- Kong, W., Zhu, J., Zhang, M., Liu, Y., Hu, J., 2018. Three-dimensional N-and S-codoped graphene hydrogel with in-plane pores for high performance supercapacitor. *Microporous Mesoporous Mater.* 268, 260–267.
- Kumar, S., Sekar, S., Kaliyamurthy, A.K., Lee, S., 2021. Bifunctional rGO-niCo₂S₄ MOF hybrid with high electrochemical and catalytic activity for supercapacitor and nitroarene reduction. *J. Mater. Res. Technol.* 12, 2489–2501.
- Li, Z., Lv, H., Wang, Z., Gu, A., He, X., Wang, L., 2019. In situ growth of CuCo₂S₄ nanocrystals on N, S-codoped reduced graphene oxide nanosheets for supercapacitors. *Mater. Res. Express* 6, 085523.
- Li, B., Yuan, F., He, G., Han, X., Wang, X., Qin, J., Guo, Z.X., Lu, X., Wang, Q., Parkin, I.P., 2017. Ultrasmall CuCo₂S₄ nanocrystals: All-in-one theragnosis nanopatform with magnetic resonance/near-infrared imaging for efficiently photothermal therapy of tumors. *Adv. Funct. Mater.* 27, 1606218.
- Li, Y., Zhang, D., Zhang, Y., He, J., Wang, Y., Wang, K., Xu, Y., Li, H., Wang, Y., 2020. Biomass-derived microporous carbon with large micropore size for high-performance supercapacitors. *J. Power Sources* 448, 227396.
- Liu, J., Chen, X., Zhu, Y., Chen, R., Yuan, W., 2021. NiCo₂S₄/nitrogen and sulfur dual-doped three-dimensional holey-reduced graphene oxide composite architectures as high-rate battery-type cathode materials for hybrid supercapacitors. *Vacuum* 190, 110302.
- Liu, C., Yu, Z., Neff, D., Zhamu, A., Jang, B.Z., 2010. Graphene-based supercapacitor with an ultrahigh energy density. *Nano Lett.* 10, 4863–4868.
- Lu, T., Zhang, Y., Cheng, C., Wang, Y., Zhu, Y., 2020. One-step synthesis of recoverable CuCo₂S₄ anode material for high-performance Li-ion batteries. *Front. Chem. Sci. Eng.* 14, 595–604.
- Luo, X., Shao, J., He, P., Zhong, M., Wang, Q., Li, K., Zhao, W., 2020. Metal organic framework derived CoS₂@Ni(OH)₂ core-shell structure nanotube arrays for high-performance flexible hybrid supercapacitors. *Electrochim. Acta* 354, 136679.
- Ma, J., Yamamoto, Y., Su, C., Badhulika, S., Fukuhara, C., Kong, C.Y., 2021. One-pot microwave-assisted synthesis of porous reduced graphene oxide as an electrode material for high capacitance supercapacitor. *Electrochim. Acta* 386, 138439.
- Mehare, R.S., Ranganath, S.P., Chaturvedi, V., Badiger, M.V., Shelke, M.V., 2018. In situ synthesis of nitrogen-and sulfur-enriched hierarchical porous carbon for high-performance supercapacitor. *Energy Fuels* 32, 908–915.
- Mohanty, A., Jaihindh, D., Fu, Y.-P., Senanayak, S.P., Mende, L.S., Ramadoss, A., 2021. An extensive review on three dimension architectural metal-organic frameworks towards supercapacitor application. *J. Power Sources* 488, 229444.
- Oda, T., Shirai, M., Suzuki, N., Motizuki, K., 1995. *J. Phys.: Condens. Matter* 7, 4433.
- Park, S.H., Park, H.J., Son, S.G., Kim, D.S., Kim, S.J., Suh, H., Ryu, T., Jeong, J.-M., Choi, B.G., 2021. Compact and porous 3D MnO₂/holey graphene films for high areal and volumetric performance in supercapacitors with high-thick electrodes. *FlatChem* 29, 100268.
- Periyasamy, G., Annamalai, K., Patil, I.M., Kakade, B., 2021. Sulfur and nitrogen co-doped rGO sheets as efficient electrocatalyst for oxygen reduction reaction in alkaline medium. *Diam. Relat. Mater.* 114, 108338.
- Pham, C.V., Eck, M., Krueger, M., 2013. Thiol functionalized reduced graphene oxide as a base material for novel graphene-nanoparticle hybrid composites. *Chem. Eng. J.* 231, 146–154.
- Qian, J., Wang, Y., Chen, Z., Liu, C., Zhou, Y., Yang, Y., Kong, B., 2019. Three dimensional Mn₃O₄-CeO₂/holey-graphene hierarchical architectures from stem for high-performance asymmetric supercapacitors. *Inorg. Chem. Commun.* 104, 8–13.
- Sahoo, S., Mondal, R., Late, D.J., Rout, C.S., 2017. Electrodeposited nickel cobalt manganese based mixed sulfide nanosheets for high performance supercapacitor application. *Microporous Mesoporous Mater.* 244, 101–108.
- Sethi, M., Shenoy, U.S., Bhat, D.K., 2021. Simple solvothermal synthesis of porous graphene-nio nanocomposites with high cyclic stability for supercapacitor application. *J. Alloys Compd.* 854, 157190.
- Singh, A., Ojha, S.K., Singh, M., Ojha, A.K., 2020. Controlled synthesis of NiCo₂S₄@NiCo₂O₄ core@ shell nanostructured arrays decorated over the rGO sheets for high-performance asymmetric supercapacitor. *Electrochim. Acta* 349, 136349.
- Sun, Y., Wu, Q., Shi, G., 2011. Graphene based new energy materials. *Energy Environ. Sci.* 4, 1113–1132.
- Takesue, M., Tomura, T., Yamada, M., Hata, K., Kuwamoto, S., Yonezawa, T., 2011. Size of elementary clusters and process period in silver nanoparticle formation. *J. Am. Chem. Soc.* 133, 14164–14167.
- Tang, J., Wang, T., Salunkhe, R.R., Alshehri, S.M., Malgras, V., Yamauchi, Y., 2015. Three-dimensional nitrogen-doped hierarchical porous carbon as an electrode for high-performance supercapacitors. *Chem. Eur. J.* 21, 17293–17298.
- Tian, Y., Yu, Z., Cao, L., Zhang, X.L., Sun, C., Wang, D.-W., 2021. Graphene oxide: An emerging electromaterial for energy storage and conversion. *J. Energy Chem.* 55, 323–344.
- Tiruneh, S.N., Kang, B.K., Kwag, S.H., Lee, Y., Kim, M., Yoon, D.H., 2018. Synergistically active NiCo₂S₄ nanoparticles coupled with holey defect graphene hydrogel for high-performance solid-state supercapacitors. *Chem. Eur. J.* 24, 3263–3270.
- Wang, X., Li, X., Zhang, L., Yoon, Y., Weber, P.K., Wang, H., Guo, J., Dai, H., 2009. N-doping of graphene through electrothermal reactions with ammonia. *Science* 324, 768–771.
- Wang, T., Wang, L.-X., Wu, D.-L., Xia, W., Jia, D.-Z., 2015. Interaction between nitrogen and sulfur in co-doped graphene and synergetic effect in supercapacitor. *Sci. Rep.* 5, 1–9.
- Wu, N., Bai, X., Pan, D., Dong, B., Wei, R., Naik, N., Patil, R.R., Guo, Z., 2021. Recent advances of asymmetric supercapacitors. *Adv. Mater. Interfaces* 8, 2001710.
- Wu, L., Sun, L., Li, X., Zhang, Q., Zhang, Y., Gu, J., Wang, K., Zhang, Y., 2020. CuCo₂S₄-rGO microflowers: First-principle calculation and application in energy storage. *Small* 16, 2001468.
- Xu, W., Liang, Y., Su, Y., Zhu, S., Cui, Z., Yang, X., Inoue, A., Wei, Q., Liang, C., 2016. Synthesis and properties of morphology controllable copper sulphide nanosheets for supercapacitor application. *Electrochim. Acta* 211, 891–899.
- Xu, Y., Lin, Z., Zhong, X., Huang, X., Weiss, N.O., Huang, Y., Duan, X., 2014. Holey graphene frameworks for highly efficient capacitive energy storage. *Nature Commun.* 5, 1–8.
- Yang, X., He, X., Li, Q., Sun, J., Lei, Z., Liu, Z.-H., 2021. 3D Hierarchical NiCo₂S₄ nanoparticles/carbon nanotube sponge cathode for highly compressible asymmetric supercapacitors. *Energy Fuels* 35, 3449–3458.
- You, H., Fang, J., 2016. Particle-mediated nucleation and growth of solution-synthesized metal nanocrystals: A new story beyond the LaMer curve. *Nano Today* 11, 145–167.
- Yu, X.Y., Lou, X.W., 2018. Mixed metal sulfides for electrochemical energy storage and conversion. *Adv. Energy Mater.* 8, 1701592.
- Zhang, Y.Z., Cheng, T., Wang, Y., Lai, W.Y., Pang, H., Huang, W., 2016. A simple approach to boost capacitance: Flexible supercapacitors based on manganese oxides@MOFs via chemically induced in situ self-transformation. *Adv. Mater.* 28, 5242–5248.
- Zhang, B.-X., Gao, H., Li, X.-L., 2014. Synthesis and optical properties of nitrogen and sulfur co-doped graphene quantum dots. *J. Chem.* 38, 4615–4621.
- Zhang, Y., Li, L., Su, H., Huang, W., Dong, X., 2015. Binary metal oxide: Advanced energy storage materials in supercapacitors. *J. Mater. Chem. A* 3, 43–59.
- Zhang, K., Wei, Y., Huang, J., Xiao, Y., Yang, W., Hu, T., Yuan, K., Chen, Y., 2020. A generalized one-step in situ formation of metal sulfide/reduced graphene oxide nanosheets toward high-performance supercapacitors. *Sci. China Mater.* 63, 1898–1909.
- Zheng, J., Lin, Z., Liu, W., Wang, L., Zhao, S., Yang, H., Zhang, L., 2014. One-pot synthesis of CuFe₂O₄ magnetic nanocrystal clusters for highly specific separation of histidine-rich proteins. *J. Mater. Chem. B* 2, 6207–6214.
- Zhou, M., Lu, F., Shen, X., Xia, W., He, H., Zeng, X., 2015. One-pot construction of three dimensional CoMoO₄/Co₃O₄ hybrid nanostructures and their application in supercapacitors. *J. Mater. Chem. A* 3, 21201–21210.

Zhu, Y., An, S., Sun, X., Cui, J., Zhang, Y., He, W., 2020. Flower-like Y-doped α -Ni(OH)₂/graphene heterostructure as advanced electrodes for high performance supercapacitor. *Vacuum* 172, 109055.

Zhu, M., Meng, D., Wang, C., Diao, G., 2013. Facile fabrication of hierarchically porous CuFe₂O₄ nanospheres with enhanced capacitance property. *ACS Appl. Mater. Interfaces* 5, 6030–6037.

Zhu, Y., Murali, S., Cai, W., Li, X., Suk, J.W., Potts, J.R., Ruoff, R.S., 2010. Graphene and graphene oxide: Synthesis, properties, and applications. *Adv. Mater.* 22, 3906–3924.

Zhu, J., Yang, D., Yin, Z., Yan, Q., Zhang, H., 2014. Graphene and graphene-based materials for energy storage applications. *Small* 10, 3480–3498.